

光学学报

基于干涉增强型混合光波导的高灵敏折射率传感器

鹿姚, 陈或芳, 万洪丹*, 梁中伟, 陈新玉, 邓玲玲

南京邮电大学电子与光学工程学院、柔性电子(未来技术)学院, 江苏 南京 210023

摘要 本文提出并研究了一种基于干涉增强型混合光波导(IE-HOW)的高灵敏折射率传感器。IE-HOW 包括微纳 U 型光波导与微瓶腔,通过光纤熔融拉锥以及电弧放电方法制备并级联而成。基于强倏逝场效应,实现了对折射率的高灵敏传感测试。实验结果表明,当微纳 U 型光纤锥区直径为 $4.88\ \mu\text{m}$ 时,IE-HOW 的折射率灵敏度相比于普通单个无干涉增强微纳 U 型光波导提高了 3 倍,高达 $8813.26\ \text{nm}/\text{RIU}$ (灵敏度单位),线性度 $R^2 > 0.9$ 。该传感器具有灵敏度高、损耗低、结构紧凑、稳定性好等优点,在环境监测、生化检测、临床诊断等领域有着广阔的应用前景。

关键词 干涉增强型混合光波导; 光纤折射率传感; 倏逝场效应; 高灵敏度

中图分类号 TN253

文献标志码 A

DOI: 10.3788/AOS231252

1 引言

光纤波导传感器由于其低成本、小体积、易操作、便于集成、高灵敏度、高稳定性、不易受电磁干扰和抗腐蚀等优势^[1],广泛用于温度、pH、湿度和振动等物理量的监测^[2-4]。其中,光纤波导折射率(RI)传感器感知由环境扰动或生化分子作用引起的细微环境 RI 的变化^[5],通过测量光谱信号的波长、功率等变化获得被测对象的特性,实现 RI 的有效解调^[6],在环境监测、生物医学和化学诊断等领域具有潜在的应用价值。

目前,不同结构的光纤波导 RI 传感器被提出,主要包括光纤光栅^[5,7]、马赫-曾德尔干涉仪(MZI)、法布里-珀罗干涉仪(FPI)^[8-10]、D 型光纤^[11]等。2020 年,Zhang 等^[5]利用飞秒激光脉冲逐点法制备长周期光栅,实现了灵敏度为 $-582.50\ \text{nm}/\text{RIU}$ (灵敏度单位)的 RI 传感。2021 年,Chen 等^[7]基于单模光纤波导包层刻蚀布拉格光栅,得到 RI 灵敏度为 $10.30\ \text{nm}/\text{RIU}$ 。2022 年,Gu 等^[9]基于游标效应提出一种大倾角光纤光栅 Sagnac 干涉环型 RI 传感器,灵敏度达到 $-1286.40\ \text{nm}/\text{RIU}$ 。同年,本文课题组提出一种基于光反射耦合式探针的 RI 传感器,灵敏度高达 $7859.27\ \text{nm}/\text{RIU}$ ^[8]。2023 年,Zhang 等^[10]基于少模-无芯-少模光纤结构,实现了灵敏度为 $345\ \text{nm}/\text{RIU}$ 的 RI

传感。

近年来,U 型光纤波导因其结构紧凑、制备简单、灵敏度高以及性能稳定等特点,成为光纤波导传感领域的研究热点^[12-13]。为进一步提高 U 型光纤波导传感器的灵敏度,一方面通过设计、优化光纤波导结构制备参数,例如对光纤波导进行熔融拉锥或引入多模光纤等,增强倏逝波与外界环境的互作用^[14]。另一方面,将新型二维材料与 U 型光纤波导结合,利用金(Au)、银(Ag)等贵金属材料激发等离子共振效应,而二硫化钼(MoS_2)、氧化石墨烯(GO)等具有大比表面积和强吸附能力,可有效增强传感单元对外部环境的敏感性^[15-17]。2021 年,Wang 等^[15]提出了一种基于级联 U 型多模、单模光纤波导的双通道表面等离子体共振光纤生物传感器,RI 灵敏度达到 $5351.40\ \text{nm}/\text{RIU}$ 。2022 年,Sun 等^[16]将 MoS_2 与微纳 U 型波导结合,RI 灵敏度为 $1660.73\ \text{nm}/\text{RIU}$ 。然而,贵金属材料损耗大、制备成本高,二维材料的响应波长受到限制,实现低成本、便于操作、高稳定性和高灵敏度的光纤波导传感器仍具有较大挑战。

本文创新性地提出并实现了一种基于干涉增强型混合光波导(IE-HOW)的高灵敏 RI 传感器。在微纳 U 型光波导的下锥区级联微瓶腔(MBC),基于较强的倏逝场效应,结合特殊的椭球型结构,具有较强集光能

收稿日期: 2023-07-10; 修回日期: 2023-08-07; 录用日期: 2023-08-16; 网络首发日期: 2023-09-22

基金项目: 国家自然科学基金(12174199,11704199)、中国博士后科学基金(2021M701765)、江苏省自然科学基金面上项目(BK20221330)、江苏大学“青蓝工程”基金、江苏省研究生科研与实践创新项目基金(KYCX22_0911,KYCX22_0912,KYCX23_0972)

通信作者: *hdwan@njupt.edu.cn

力的同时,引入MBC增加了干涉长度,并进一步增强了模场干涉效应。当外界折射率环境变化时,纤芯模式和包层模式之间的相位差也发生改变,从而引起IE-HOW的透射光谱发生变化。实验结果表明,相比于普通无干涉增强微纳U型光纤光波导(UOW),IE-HOW的RI灵敏度最高提高了~3倍,达到8813.26 nm/RIU,线性度 $R^2 > 0.9$ 。该传感器具有灵敏度高、温度影响小、稳定性好、结构简单和成本低等优势,通过采取一些物理、化学表面功能化方式结合探针、蛋白等具有特异性识别功能的特殊物质,或者结合一些新型材料如二维碳纳米材料、三维框架结构、金属材料等可进行化学生物传感实验,在环境监测、生化检测以及医学诊断领域具有良好的应用前景。

2 基本原理

本文提出的IE-HOW示意图如图1(a)所示。该传感器由UOW和MBC级联构成。 R 、 d 分别为IE-HOW的曲率直径和锥区直径, L_0 为MBC长度。当光由入射端port 1注入,随着光纤波导直径变小光场逐渐泄漏至包层中。当光达到光纤波导的弯曲区域,由

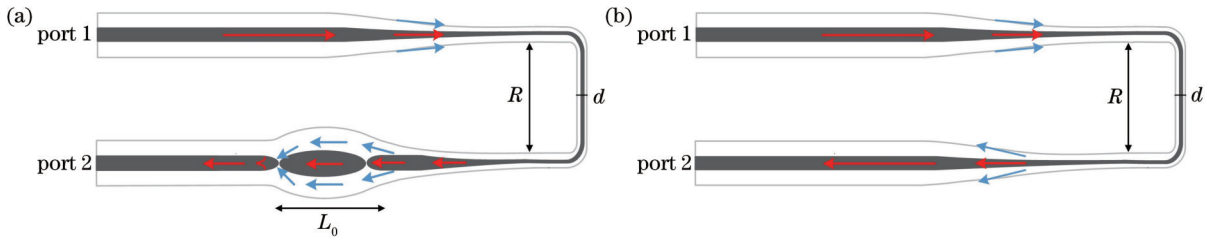


图1 传感器结构示意图。(a)IE-HOW;(b)UOW

Fig. 1 Schematic diagram of sensor structure. (a) IE-HOW; (b) UOW

当 $\Delta\varphi = (2N+1)\pi$, N 为整数时,则会发生相干相消干涉,干涉谷的波长为

$$\lambda_0 = \frac{2\Delta n_{\text{eff}} L}{2N+1}. \quad (3)$$

由式(3)可知,光谱的干涉波长与 L 和 Δn_{eff} 成正比。当外界环境或干涉长度发生变化时,干涉波长会发生偏移,波长灵敏度表示为

$$\frac{d\lambda_0}{dn_{\text{ext}}} = -\frac{\lambda_0}{G} \frac{\partial n_{\text{eff}}^{\text{clad}}}{\partial n_{\text{ext}}}, \quad (4)$$

式中: $G = \Delta n_{\text{eff}} \left[1 - \frac{\lambda_0}{\Delta n_{\text{eff}}} \left(\frac{\partial n_{\text{eff}}^{\text{core}}}{\partial \lambda} - \frac{\partial n_{\text{eff}}^{\text{clad}}}{\partial \lambda} \right) \right]$; n_{ext} 为外界环境折射率。由式(3)可知,纤芯和包层的有效RI差增大导致波长红移,且长波长处传感灵敏度高。

自由光谱范围(FSR, F_{SR})表示为

$$F_{\text{SR}} = \frac{\lambda_0^2}{\Delta n_{\text{eff}} L}. \quad (5)$$

根据式(5)可知, F_{SR} 与干涉长度 L 和有效RI差成反比。

于全反射条件被破坏,部分纤芯光场进一步泄漏至包层中,增强倏逝场效应。同时,较大的弯曲直径使得光场的损耗降低。由于较小的级联长度差,当光场到达锥形光纤过渡区时立即被MBC收集,在内部传播并产生干涉,透射光谱由port 2输出并记录。图1(b)为UOW的示意图,port 1入射的光场经过弯曲区域后,大部分光场沿着光纤传输至port 2端记录,还有小部分包层中的光场会泄漏到空气中,增加损耗。

纤芯模和包层模分别以 I_{core} 和 I_{clad} 的强度进入IE-HOW,其干涉强度^[18]可表示为

$$I = I_{\text{core}} + I_{\text{clad}} + 2\sqrt{I_{\text{core}} I_{\text{clad}}} \cos \Delta\varphi, \quad (1)$$

式中, $\Delta\varphi$ 表示纤芯模和包层模之间的相位差,其计算公式^[19]为

$$\Delta\varphi = \frac{2\pi\Delta n_{\text{eff}} L}{\lambda_0} = \frac{2\pi}{\lambda_0} (n_{\text{eff}}^{\text{core}} - n_{\text{eff}}^{\text{clad}}) L, \quad (2)$$

式中: λ_0 表示干涉峰波长; Δn_{eff} 为纤芯和包层模的有效RI差, $\Delta n_{\text{eff}} = n_{\text{eff}}^{\text{core}} - n_{\text{eff}}^{\text{clad}}$, $n_{\text{eff}}^{\text{core}}$ 和 $n_{\text{eff}}^{\text{clad}}$ 分别为纤芯和包层模的有效RI; L 、 L_1 和 L_0 分别为IE-HOW、UOW和MBC的干涉长度, $L = L_1 + L_0$ 。

图2所示为采用光束传播算法仿真模拟不同 d 下UOW和IE-HOW中光场能量的传输与交换过程。入射波长设置为1550 nm,网格尺寸为0.1 μm ,包层、纤芯、环境RI分别为1.456、1.461、1.000。光场沿着 z 轴自下而上传播,通过改变 d 监视光纤波导中的光场能量分布。图2(a)~2(c)分别为 $d=8 \mu\text{m}$ 、 $d=6 \mu\text{m}$ 、 $d=4 \mu\text{m}$ 的UOW锥区部分光场能量分布图,从图中可知,由于芯径不匹配,光场能量在通过锥形区域后部分光场形成发散状泄漏至空气中增加了损耗, d 越小,能量泄漏越多,倏逝场增强,与外部环境的相互作用增强。图2(d)~2(f)分别为 $d=8 \mu\text{m}$ 、 $d=6 \mu\text{m}$ 、 $d=4 \mu\text{m}$ 的IE-HOW锥区部分光场能量分布图,随着直径逐渐减小,倏逝场泄漏逐渐增强,通过锥区后的光场不再出现发散状的光场,而是会聚到尾端的MBC中。可见UOW后端级联MBC可将扩散的光场有效收集,提高参与干涉的光场能量占比,增强干涉。相比于UOW,IE-HOW具有较强的干涉效应以及较小的光场传输损耗,可实现高灵敏、低损耗RI传感。

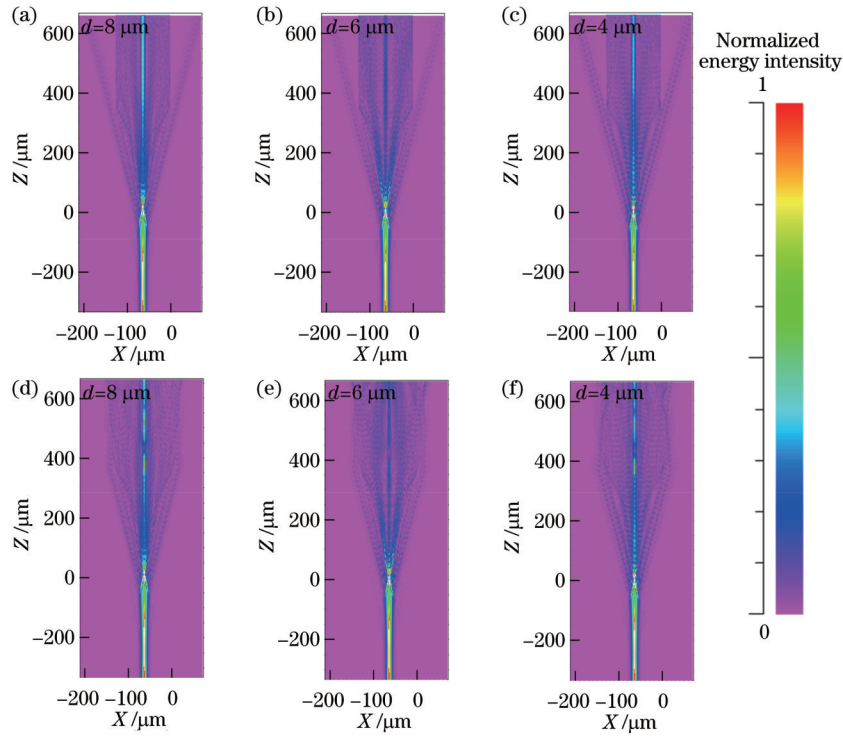


图 2 UOW 和 IE-HOW 在不同 d 条件下的光场分布仿真分析结果。UOW: (a) $d=8 \mu\text{m}$ 、(b) $d=6 \mu\text{m}$ 、(c) $d=4 \mu\text{m}$; IE-HOW: (d) $d=8 \mu\text{m}$ 、(e) $d=6 \mu\text{m}$ 、(f) $d=4 \mu\text{m}$

Fig. 2 Simulation analysis results of light field distributions under different d for UOW and IE-HOW. UOW: (a) $d=8 \mu\text{m}$, (b) $d=6 \mu\text{m}$, and (c) $d=4 \mu\text{m}$; IE-HOW: (d) $d=8 \mu\text{m}$, (e) $d=6 \mu\text{m}$, and (f) $d=4 \mu\text{m}$

3 实验

3.1 器件制备

采用氢氧焰熔融拉锥和电弧放电的方法制备 UOW 以及 IE-HOW。图 3(a) 为 IE-HOW 的制备过程。使用电弧放电的方式在单模光纤 (SMF, 纤芯/包层直径为 $8/125 \mu\text{m}$) 表面熔接一个 MBC, 通过控制熔接机 (DVP-740) 放电次数和推进量来控制 MBC 的大小。再将含有 MBC 的 SMF 放置在氢氧焰拉锥机上熔融拉锥, 精确控制并优化氢气流量、步进速度 (v)、拉伸

长度 (h) 等参量。最后, 将拉锥过后的混合光波导弯曲成 U 形, 合理控制弯曲直径 (R), 减少弯曲损耗。UOW 主要由通过对 SMF 熔融拉锥后弯曲操作制备而成。图 3(b) 为 MBC 的显微图像, 直径 $D \sim 212 \mu\text{m}$ 、长度 $L_0 \sim 570.93 \mu\text{m}$, 插图为 IE-HOW 的实物图, $R \sim 12 \text{mm}$ 。保持 MBC 尺寸及 R 不变, 改变拉伸长度 ($h=16000 \mu\text{m}$ 、 $h=18000 \mu\text{m}$ 、 $h=20000 \mu\text{m}$) 分别制备不同锥区直径 ($d_1=12.30 \mu\text{m}$ 、 $d_2=7.44 \mu\text{m}$ 、 $d_3=4.88 \mu\text{m}$) 的 UOW 和 IE-HOW。

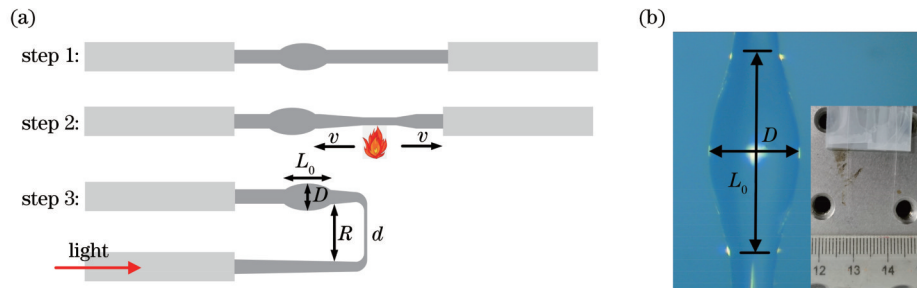


图 3 器件制备。(a) IE-HOW 制备过程; (b) MBC 显微镜图像 (插图为 IE-HOW 实物图)

Fig. 3 Fabrication of devices. (a) Preparation progress of IE-HOW; (b) microscope image of MBC (Insert is physical image of IE-HOW)

3.2 实验装置

图 4 为基于 IE-HOW 的 RI 传感实验装置图, 包括宽带光源 (BBS, $1250 \sim 1650 \text{nm}$)、样液池、高精度位移

平台以及光谱分析仪 (OSA, AQ6370D)。BBS 发出的光进入传感单元, 输出干涉信号由 OSA 收集。

使用去离子水配置不同浓度的 NaCl 溶液, 以形成

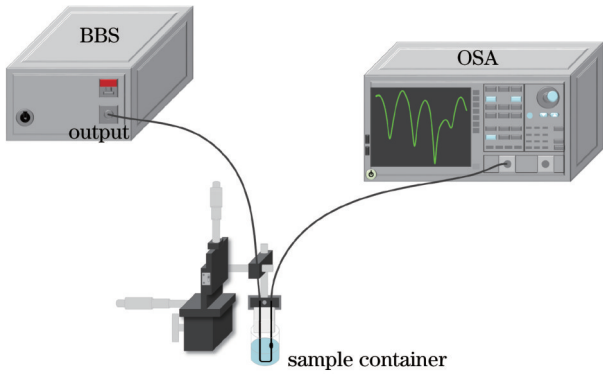


图 4 基于 IE-HOW 的 RI 传感实验装置图

Fig. 4 Experimental setup for RI sensing based on IE-HOW

不同 RI 的待测溶液, 利用阿贝折射仪多次测试并标定各浓度 RI。使用高精度位移平台控制传感单元, 按照从低浓度到高浓度的顺序依次浸入 NaCl 溶液中实现

RI 传感测试。每次更换 RI 溶液前用去离子水清洗传感单元, 保证测试结果的准确性。

4 分析与讨论

4.1 UOW 的 RI 测试结果

为证明 MBC 在 IE-HOW 中的干涉增强效应, 首先将 UOW 置于传感系统中测试其 RI 灵敏度。图 5(a)、5(c)、5(e) 分别为不同 RI 下不同直径 (d_1 、 d_2 、 d_3) 的 UOW 的透射光谱。结果表明, 随着 RI 由 1.333 逐渐增大至 1.362, 光谱逐渐红移。分别选取透射谱不同波段中的三个干涉谷 (dip 1, dip 2, dip 3) 进行数据拟合, 由于 d 不同, 导致纤芯和包层有效 RI 差发生变化, 从而导致不同 d 结构透射谱中的干涉谷对应的干涉波长会有所变化, 选取波段相近的干涉波谷进行数据处理。图 5(b)、5(d)、5(f) 分别为 RI 与光谱波长的拟合关系曲线图, 由图中可知, 长波长的 RI 灵敏度高

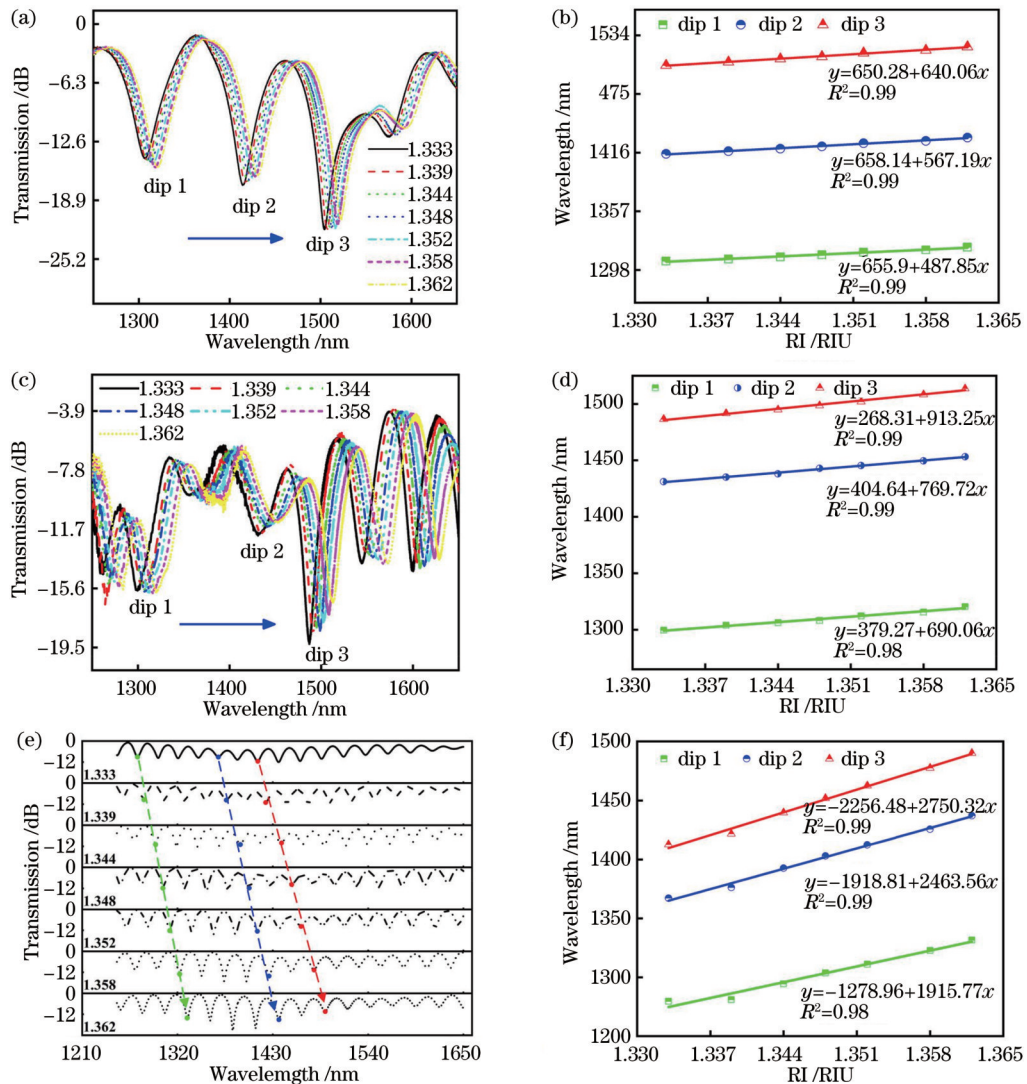


图 5 基于 UOW 的 RI 传感实验结果。不同 RI 下的透射光谱: 直径为 (a) d_1 ; (c) d_2 ; (e) d_3 ; 波长与 RI 的拟合关系曲线: 直径为 (b) d_1 ; (d) d_2 ; (f) d_3

Fig. 5 Experimental results of RI sensing based on UOW. Transmission spectra at different RI: diameters are (a) d_1 ; (c) d_2 ; (e) d_3 ; fitting relationship curve between wavelength and RI: diameters are (b) d_1 ; (d) d_2 ; (f) d_3

于短波长处。不同直径的 UOW 对应的最大 RI 灵敏度分别为 640.06 nm/RIU (1507.5 nm)、913.25 nm/RIU (1487.1 nm)、2750.32 nm/RIU (1412.7 nm), 线性度 $R^2 > 0.9$ 。

4.2 IE-HOW 的 RI 测试结果

基于 IE-HOW 的 RI 测试结果如图 6 所示。

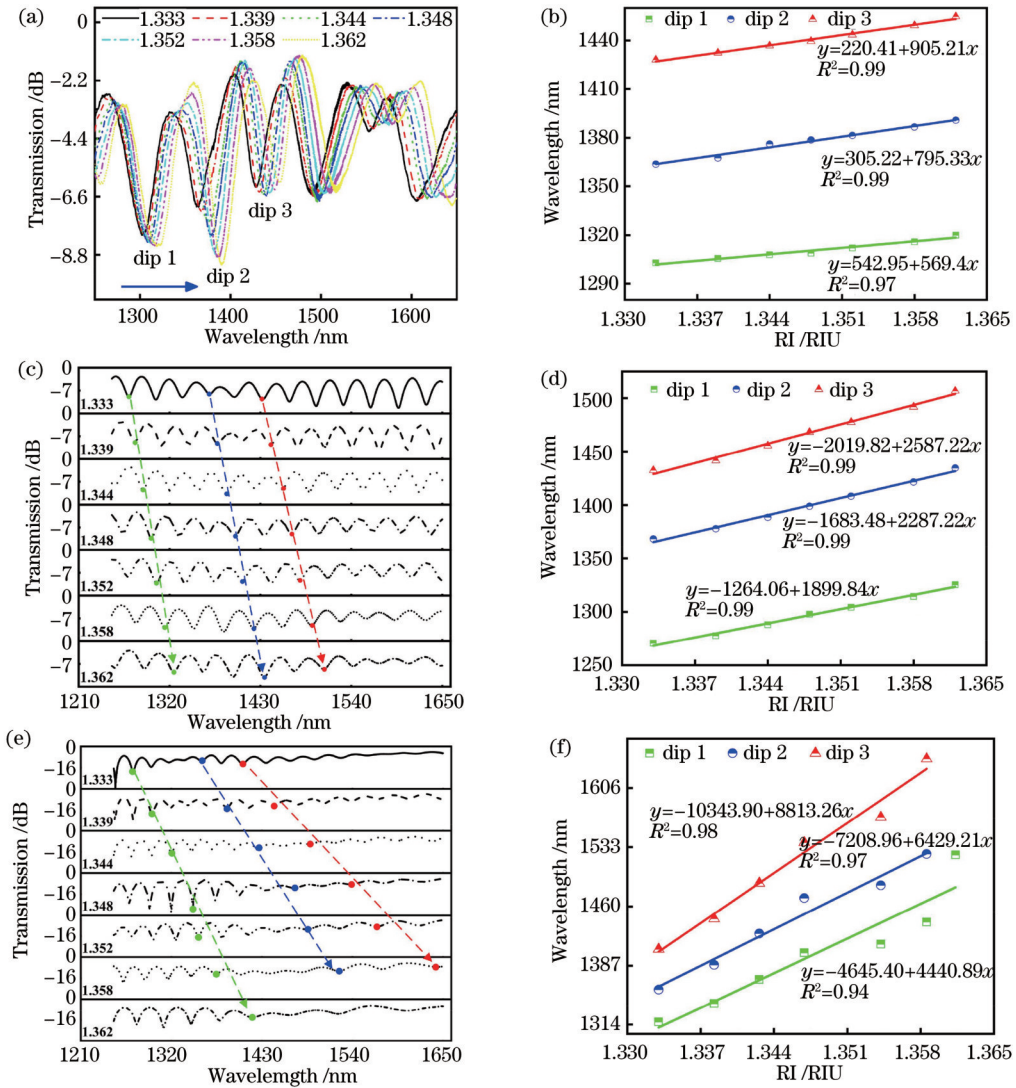


图 6 基于 IE-HOW 的 RI 传感实验结果。不同 RI 下的透射光谱: 直径为 (a) d_1 ; (c) d_2 ; (e) d_3 ; 波长与 RI 的拟合关系曲线: 直径为 (b) d_1 ; (d) d_2 ; (f) d_3

Fig. 6 Experimental results of RI sensing based on IE-HOW. Transmission spectra at different RI: diameters are (a) d_1 ; (c) d_2 ; (e) d_3 ; fitting relationship curve between wavelength and RI: diameters are (b) d_1 ; (d) d_2 ; (f) d_3

图 7 为不同 d 下 UOW 和 IE-HOW 的最大 RI 灵敏度对比结果, d 越小, RI 灵敏度越大。与 UOW 相比, IE-HOW 的 RI 传感灵敏度最高可提高 ~ 3 倍。

4.3 IE-HOW 温度测试及稳定性测试结果

为评估温度带来的交叉敏感影响, 实验测试了 IE-HOW (d_3) 的温度响应和环境稳定性。将 IE-HOW 放置在温控箱中, 温度调谐范围为 20~80 °C, 间隔 10 °C 并稳定 10 min 记录数据, 选取三个不同波长处干涉峰

图 6(a)、6(c)、6(e) 为不同 RI、不同直径 (d_1 、 d_2 、 d_3) 下的透射光谱, 随着 RI 由 1.333 逐渐增大至 1.362, 光谱产生红移。图 6(b)、6(d)、6(f) 为光谱波长与 RI 的拟合关系曲线, 最大 RI 灵敏度分别为 905.21 nm/RIU (1428.10 nm)、2587.22 nm/RIU (1432.50 nm)、8813.26 nm/RIU (1406.50 nm), 线性度 $R^2 > 0.9$ 。

dip 1、dip 2、dip 3, 其光谱波长漂移量与温度变化曲线如图 8(a) 所示, 插图为对应光谱波谷的细节放大图。由实验结果可知, 60 °C 范围内的波长变化量 < 0.02 nm, 该 RI 传感器具有较低的温度影响。图 8(b) 为 IE-HOW 的稳定性测试结果, 插图为对应波谷的细节放大图。三个干涉峰 dip 1、dip 2、dip 3 的波长变化量随时间波动结果如图 8(b) 所示, 1 h 内波长最大变化量 < 0.02 nm, 因此, 该 RI 传感器具有较高的稳

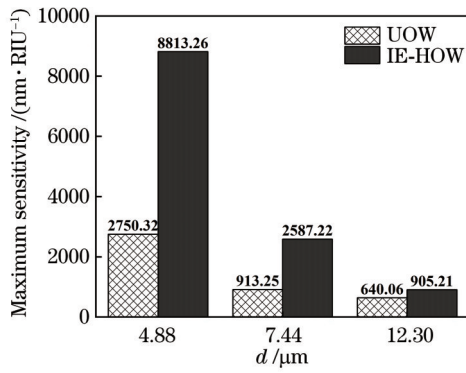


图7 不同 d 下 UOW 和 IE-HOW 的最大 RI 灵敏度对比
Fig. 7 Comparison of maximum RI sensitivity of UOW and IE-HOW under different d

表 1 不同类型 U 型 RI 传感器的灵敏度比较

Table 1 Sensitivity comparison of different types of U-shaped RI sensors

Structure	Sensitivity / (nm·RIU ⁻¹)	Reference
Single mode U-shaped fiber	207.00	[12]
Taper single-mode U-shaped fiber	1556.27	[14]
Multimode fiber-single mode fiber-multimode fiber U-shaped	5351.40	[15]
Polishing U	1307.60	[17]
Long period fiber grating cascaded U-shaped fiber	61.99	[20]
U-shaped tapered arm cascade of multimode fiber	4816.09	[21]
IE-HOW	8813.26	This work

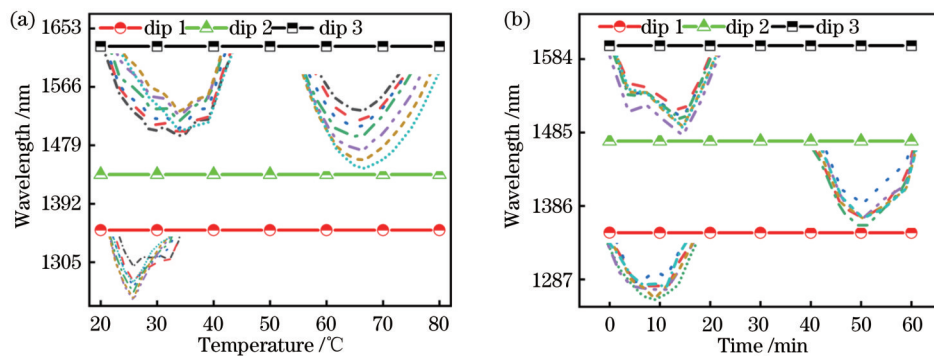


图 8 基于 IE-HOW 的温度响应和稳定性测试。(a) 不同温度下的光谱波长; (b) 1 h 内的波长稳定性 (插图是结构的透射光谱)
Fig. 8 Temperature response and stability test based on IE-HOW. (a) Spectral wavelengths at different temperatures; (b) wavelength stability within 1 h (Insert is transmission spectrum of structure)

参 考 文 献

[1] Zhao Y, Li X G, Zhou X, et al. Review on the graphene based optical fiber chemical and biological sensors[J]. Sensors and Actuators B: Chemical, 2016, 231: 324-340.

[2] Lin Y, Chen S, Wang M L, et al. Fiber-optic fast response pH sensor in fiber Bragg gating using intelligent hydrogel coatings [J]. Optical Engineering, 2015, 54(5): 057107.

[3] Fu X H, Zhang X C, Li J X, et al. A cascaded temperature sensor based on few mode fiber and Pagoda structure with five waist-enlarged tapers[J]. Optics Communications, 2023, 526: 128888.

[4] Bian C, Wang J, Bai X H, et al. Optical fiber based on humidity sensor with improved sensitivity for monitoring applications[J]. Optics & Laser Technology, 2020, 130: 106342.

[5] Zhang Y N, Jiang P, Qiao D, et al. Sensing characteristics of long period grating by writing directly in SMF-28 based on 800 nm femtosecond laser pulses[J]. Optics & Laser Technology, 2020, 121: 105839.

[6] Yan H T, Zhang C, Zhao X Y, et al. Experimental study of liquid refractive index sensing based on a U-shaped micro-fiber [J]. Optik, 2015, 126(11/12): 1254-1257.

[7] Chen Q, Wang D N, Gao F. Simultaneous refractive index and temperature sensing based on a fiber surface waveguide and fiber Bragg gratings[J]. Optics Letters, 2021, 46(6): 1209-1212.

[8] Chen Y F, Wan H D, Liang Z W, et al. Multi-parameter sensors based on optical reflective coupler probe[J]. IEEE Photonics Journal, 2022, 14(5): 6848206.

[9] 古洪, 罗彬彬, 石胜辉, 等. 基于极大倾角光纤光栅 Sagnac 游标干涉仪的折射率传感器 [J]. 光学学报, 2022, 42(20): 2006004.

- Gu H, Luo B B, Shi S H, et al. Refractive index sensor based on excessively tilted fiber grating Sagnac vernier interferometer[J]. *Acta Optica Sinica*, 2022, 42(20): 2006004.
- [10] 张静, 李永倩. 基于少模-无芯-少模光纤结构的高灵敏折射率传感器[J]. *应用光学*, 2023, 44(2): 462-468.
- Zhang J, Li Y Q. High sensitivity refractive index sensor based on a few mode coreless few mode fiber structure[J]. *Journal of Applied Optics*, 2023, 44(2): 462-468.
- [11] Li L L, Wei Y, Liu C L, et al. Dual-channel fiber-optic surface plasmon resonance sensor with cascaded coaxial dual-waveguide D-type structure and microsphere structure[J]. *Chinese Physics B*, 2023, 32(2): 020702.
- [12] 唐洁媛, 张佳佳, 曾央夫, 等. 基于 U 型弯曲光纤模间干涉的折射率传感[J]. *光子学报*, 2015, 44(5): 0506003.
- Tang J Y, Zhang Q Q, Zeng Y F, et al. Refractive index sensing based on the modal interference of U-shape bending fiber[J]. *Acta Photonica Sinica*, 2015, 44(5): 0506003.
- [13] Ge J T, Zhang Y X, Zhang W G, et al. Simultaneous measurement of RI and temperature based on compact U-shaped interferometer[J]. *IEEE Sensors Journal*, 2020, 20(7): 3593-3598.
- [14] Li H X, Liu S, Xu S M, et al. Relative humidity sensor based on U-shaped microfiber interferometer coated with MoS₂ films[J]. *Materials Letters*, 2021, 301: 130245.
- [15] Wang Q, Song H, Zhu A S, et al. A label-free and anti-interference dual-channel SPR fiber optic sensor with self-compensation for biomarker detection[J]. *IEEE Transactions on Instrumentation and Measurement*, 2021, 70: 7002007.
- [16] Sun D D, Liu S, Xu S M, et al. A U-shaped microfiber interferometer coated with MoS₂ film for simultaneous measuring relative humidity and temperature[J]. *Optical Fiber Technology*, 2022, 73: 103009.
- [17] 周建乔, 景宁, 王志斌, 等. 侧边抛磨的 U 型金溅射塑料光纤等离子体共振传感器[J]. *应用光学*, 2019, 40(3): 511-516.
- Zhou J Q, Jing N, Wang Z B, et al. Side-grinding U-shaped gold sputter plastic fiber SPR sensor[J]. *Journal of Applied Optics*, 2019, 40(3): 511-516.
- [18] Liu T G, Chen Y F, Han Q, et al. Magnetic field sensor based on U-bent single-mode fiber and magnetic fluid[J]. *IEEE Photonics Journal*, 2014, 6(6): 5300307.
- [19] 陈彧芳, 万洪丹, 陈乾, 等. 基于稀土光纤双花生结的高灵敏度光纤温度传感器[J]. *中国激光*, 2020, 47(1): 0110001.
- Chen Y F, Wan H D, Chen Q, et al. High sensitivity optical fiber temperature sensor based on rare-earth-doped double-fiber peanut[J]. *Chinese Journal of Lasers*, 2020, 47(1): 0110001.
- [20] Song H, Gao H L, Zhao X W, et al. Characteristics of novel tail ring-shaped cascaded long period fiber grating sensor[J]. *Optical Fiber Technology*, 2020, 55: 102134.
- [21] Ren Z H, Wang Q, Zhao W M, et al. A High-FOM surface plasmon resonance sensor based on MMF-TUMMF-MMF structure of optical fiber[J]. *Optical Fiber Technology*, 2022, 72: 102970.

High-Sensitivity Refractive Index Sensor Based on Interference Enhanced Hybrid Optical Waveguide

Lu Yao, Chen Yufang, Wan Hongdan*, Liang Zhongwei, Chen Xinyu, Deng Lingling

College of Electronic and Optical Engineering & College of Flexible Electronics (Future Technology), Nanjing University of Posts and Telecommunications, Nanjing 210023, Jiangsu, China

Abstract

Objective Optical fiber waveguide refractive index (RI) sensors have potential applications in environmental monitoring and biochemical sensing due to their low cost, small size, easy operation and integration, high sensitivity and stability, anti-electromagnetic interference, and corrosion resistance. At present, different optical fiber waveguide RI sensors have been proposed, among which U-shaped optical fiber waveguide has become a research hotspot in optical fiber waveguide sensing because of its compact structure, simple preparation, and high sensitivity. On one hand, the preparation parameters of optical fiber waveguide structures are designed and optimized, and on the other hand, the sensitivity of the sensing unit to the external environment is improved by combining new two-dimensional materials to further improve the sensitivity of U-shaped optical fiber waveguide sensors. However, precious metal materials have high losses and preparation costs, with limited response wavelength of two-dimensional materials. Realizing optical fiber waveguide RI sensors featuring low cost, easy operation, and high stability and sensitivity still poses significant challenges. Thus, we propose and implement an interference enhanced hybrid optical waveguide (IE-HOW). The sensor based on IE-HOW is characterized by high sensitivity, low loss, compact structure, and good stability, and it has broad application prospects in biochemical detection, clinical diagnosis, and other fields.

Methods The beam propagation method is employed to simulate the energy distribution of the optical field before and after the cascade. To prepare IE-HOW, we first fuse a micro-bottle cavity (MBC) on the surface of single mode fiber (SMF) by arc discharge, and then place the SMF containing MBC on the hydrogen-oxygen flame tapering machine for melting tapering. During the manufacturing, precise control of the discharge frequency and propulsion amount of the fusion welding machine controls the MBC size, and parameters such as hydrogen flow rate, step speed, and stretching length of the hydrogen oxygen flame cone pulling machine are controlled precisely. Finally, the bending diameter is controlled

reasonably to bend the tapered hybrid optical waveguide into a U-shaped one, and the length and diameter of the MBC are characterized by an optical microscope. The MBC size and bending diameter are kept unchanged, and the stretching lengths are changed ($h=16000\ \mu\text{m}$, $h=18000\ \mu\text{m}$, and $h=20000\ \mu\text{m}$) to prepare ordinary non-interference enhanced micro-nano U-shaped optical waveguide (UOW) and IE-HOW structures with different cone diameters respectively. Meanwhile, RI sensing tests are performed on ordinary UOW without cascaded structures and IE-HOW with cascaded structures to compare their sensitivity. For RI sensing, the change of external environment RI will alter the phase difference between the core mode and the cladding mode, leading to accordingly changed spectrum wavelength. The broadband light source (BBS, from 1250 to 1650 nm) is connected to the IE-HOW input end, and the output transmission spectrum of the output section is recorded in real time by an optical spectral analyzer (OSA, AQ6370D).

Results and Discussions Solutions with different RI are prepared by NaCl solution and calibrated with Abbe refractometer, with an RI range of 1.333–1.362. In UOW-based RI sensing measurements, the maximum sensitivities of RI sensor tests with cone diameter $d_1=12.30\ \mu\text{m}$, $d_2=7.44\ \mu\text{m}$, and $d_3=4.88\ \mu\text{m}$ are 640.06 nm/RIU (1507.5 nm), 913.25 nm/RIU (1487.10 nm), and 2750.32 nm/RIU (1412.70 nm) respectively, with the linearity $R^2 > 0.9$ (Fig. 5). In IE-HOW-based RI sensing measurements, the maximum sensitivities of RI sensor tests with cone diameter $d_1=12.30\ \mu\text{m}$, $d_2=7.44\ \mu\text{m}$, and $d_3=4.88\ \mu\text{m}$ are 905.21 nm/RIU (1428.10 nm), 2587.22 nm/RIU (1432.50 nm), and 8813.26 nm/RIU (1406.50 nm) respectively, with the linearity $R^2 > 0.9$ (Fig. 6). The smaller cone diameter leads to greater RI sensitivity. When the cone diameter of the micro-nano U-shaped fiber is $4.88\ \mu\text{m}$, the RI sensitivity of IE-HOW is three times higher than that of UOW (Fig. 7). Temperature and stability tests are carried out on IE-HOW with a cone diameter of $4.88\ \mu\text{m}$ respectively. The sensing unit is placed in a temperature control box, and spectral data are recorded at intervals of $10\ ^\circ\text{C}$ and stabilized for 10 min within the range of $20\text{--}80\ ^\circ\text{C}$. The wavelength variation within the range of $60\ ^\circ\text{C}$ is less than 0.02 nm (Fig. 8). The spectral data are recorded every 10 min at room temperature, and the maximum wavelength change within 1 h is less than 0.02 nm (Fig. 8). Therefore, the high-sensitivity RI sensor based on IE-HOW has high-temperature stability.

Conclusions We propose and implement a highly sensitive RI sensor based on IE-HOW. By cascading UOW and MBC to construct IE-HOW, interference enhancement and low loss are achieved based on the strong focusing effect of MBC and large bending diameter respectively. Compared to UOW, under the same cone diameter of $4.88\ \mu\text{m}$, the RI sensitivity is increased by 3 times, reaching 8813.26 nm/RIU, and $R^2 > 0.9$. This sensor has advantages such as high sensitivity, low loss, all fiber, low cost, and good stability, with practical significance in biosensing, environmental monitoring, and other fields that require high RI sensitivity.

Key words interference enhanced hybrid optical waveguide; optical fiber refractive index sensing; evanescent field effect; high sensitivity